Contents lists available at ScienceDirect

Inorganic Chemistry Communications

journal homepage: www.elsevier.com/locate/inoche

Short communication

A novel strategy for enhancing NO_2 sensitivity of new 1D organic–inorganic metal halide hybrids

Jie Chen [a,b], Chuanzhe Wang [a,b], Jianqiang Zhao [b], Guangling Liang [b], Gang Xu [b,c,d], Guan-E Wang [b,*]

[a] College of Chemistry, Fuzhou University, Fuzhou City, Fujian Province 350116, PR China
[b] State Key Laboratory of Structural Chemistry, Fujian Institute of Research on the Structure of Matter, Chinese Academy of Sciences, Fuzhou 350002, PR China
[c] University of Chinese Academy of Sciences, Beijing 100049, China
[d] Fujian Science & Technology Innovation Laboratory for Optoelectronic Information of China, Fuzhou, Fujian 350108, China

ARTICLE INFO

ABSTRACT

Organic-inorganic metal halide hybrids show great potential for applications in catalysis, solar cells, gas sensing, etc. Due to the highly designable structure, a novel strategy could be developed to improve their gas sensitivity in gas detection. Two new organic–inorganic metal halide hybrids have been synthesized using $[(Et)_2MP]^+$ (MP = *p*-mercaptopyridine, Et = ethyl) as the cationic template. The 1-dimensional inorganic chain provides good electron transport channels, and the electronic structure can be easily adjusted by changing the halogen to enhance the sensitivity of gas sensing. The difference in response values for NO_2 can reach 27 times before and after the halogen change. This work provides insight into the design of gas-sensing materials with improved properties.

1. Introduction

Organic-inorganic metal halide hybrids exhibit outstanding optoelectronic features such as strong light absorption, high carrier mobility, long carrier lifetime, high optical anisotropy, and low trap density [1–6]. Therefore, they show great potential application in catalysis [7–9], ferroelectricity [10–12], solar cells [13–16], light-emitting diodes [17–20], photodetectors [21–23], sensors [24–27], etc. The earlier proposal of organic–inorganic metal halide hybrid $(CH_3NH_3PbBr_3)$ nanoparticles (6.1 nm in size) for the luminescence detection of picric acid by Muthu et al. was one of the works that pioneered the sensing application of organic–inorganic metal halide hybrid [28]. Compared with fluorescence detection, chemiresistive sensors show great potential for applications with their faster detection speed and real-time detection capability. Paolo Samorì et al. synthesized a $MAPbI_3$ thin film chemiresistive oxygen sensor. The sensor can be used to detect 70 ppm oxygen at room temperature with a detection time as low as 400 ms [24]. Xu et al. synthesized a new 1D hybrid perovskite-like material $[(Me_3)DAB (Me_3)]PbI_4 \cdot H_2O$ for high-sensitivity humidity sensing with a response time of 42 s [29]. However, the gases tested by organic–inorganic metal halide hybrids are mainly ammonia and oxygen. New materials designs are needed to achieve rapid detection of other toxic and hazardous gases.

Sensitivity is the most important indicator to evaluate the performance of gas sensors. At present, there are two main strategies to improve the sensitivity, one is to increase the specific surface area of the material to increase the contact area between the material and the gas [30–32]; the other is to increase the interaction force between the material and the gas [33–35]. For example, Haibo Zeng et al. achieved efficient NO_2 sensing of SnS_2/BP (black phosphorus) by Lewis acidic modification [33]. For organic–inorganic metal hybrid halides, increasing the interaction between materials and gases is a more efficient approach due to their excellent structural designability [36].

Here we report a new edge-shared organic–inorganic metal halide hybrid $[(Et)_2MP]PbBr_3$ (MP = *p*-mercaptopyridine, Et = ethyl). The one-dimensional inorganic chains provide good electron transport channels resulting in $[(Et)_2MP]PbBr_3$ with typical semiconductor properties. The response for $[(Et)_2MP]PbBr_3$ to 100 ppm NO_2 is 18.2%. This value can be dramatically increased to 490% for $[(Et)_2MP]PbI_3$ by replacing bromine with iodine, which is 27 times as before. Mechanism studies demonstrated that the iodine ion with stronger Lewis alkalinity increases the sensitivity.

* Corresponding author.
E-mail address: gewang@fjirsm.ac.cn (G.-E. Wang).

Table 1
Crystallographic information of [(Et)$_2$MP]PbBr$_3$ and [(Et)$_2$MP]PbI$_3$.

Crystal data	[(Et)$_2$MP]PbBr$_3$	[(Et)$_2$MP]PbI$_3$
Empirical formula	C$_9$H$_{14}$Br$_3$NPbS	C$_9$H$_{14}$I$_3$NPbS
Formula weight	615.19	756.16
Temperature/K	121.00	121.00
Crystal system	orthorhombic	orthorhombic
Space group	$P2_12_12_1$	$P2_12_12_1$
a/Å	4.4115(10)	4.5683(10)
b/Å	16.8108(4)	17.4726(3)
c/Å	21.0023(4)	20.9291(4)
α/°	90	90
β/°	90	90
γ/°	90	90
V/Å^3	1557.55(6)	1670.56(6)
Z	4	4
ρ_{calc}/gcm^{-3}	2.623	3.006
μ/mm^{-1}	20.811	43.496
F(000)	1112.0	1328.0
Radiation	Ga-$K\alpha$	Ga-$K\alpha$
	($\lambda = 1.3405$)	($\lambda = 1.3405$)
Reflections collected	6594	12,902
Independent reflections	3257	3610
	[R_{int} = 0.0346]	[R_{int} = 0.0379]
Data/restraints/parameters	3257/0/139	3610/0/139
2theta range for data collection/°	5.854 to 120.38	5.728 to 121.452
Index ranges	$-5 \leq h \leq 2$,	$-5 \leq h \leq 5$,
	$-21 \leq k \leq 21$,	$-22 \leq k \leq 22$,
	$-27 \leq l \leq 26$	$-27 \leq l \leq 24$
GOF on F^2	0.971	1.066
Final R indexes [$I>=2\sigma$ (I)]	$R_1 = 0.0357$,	$R_1 = 0.0317$,
	$wR_2 = 0.0778$	$wR_2 = 0.0730$
Final R indexes [all data]	$R_1 = 0.0434$,	$R_1 = 0.0376$,
	$wR_2 = 0.0813$	$wR_2 = 0.0763$

2. Experimental section

2.1. Material

Lead bromide (PbBr$_2$), lead(II) iodide (PbI$_2$), 4,4′-Dithiodipyridine (DTDP), p-mercaptopyridine (MP), hydroiodic acid (HI), hydrobromic acid (HBr) and ethanol (EtOH) were purchased from Adamas-beta. All solvents and reagents were purchased without further purification.

2.2. Synthesis of [(Et)$_2$MP]PbBr$_3$ and [(Et)$_2$MP]PbI$_3$

The crystals of [(Et)$_2$MP]PbBr$_3$ and [(Et)$_2$MP]PbI$_3$ were grown by the solvothermal method. [(Et)$_2$MP]PbBr$_3$ was prepared by mixing PbBr$_2$ (0.2 mmol, 73.4 mg) and DTDP (0.5 mmol, 110.0 mg) in 5 mL EtOH first, and 1 mL HBr (45%) was added at room temperature. The average yield of the crystal (relative to the metal) was 81%. Then the mixture was transferred to a 25 mL Teflon-lined reaction vessel and kept at 150 °C for 72 h. After gently cooling to room temperature, white rod-shaped crystals of [(Et)$_2$MP]PbBr$_3$ were obtained. And purification was achieved by washing with ethanol five times before vacuum drying at 60 °C for 12 h. Yellowish needle-shaped crystals of [(Et)$_2$MP]PbI$_3$ can be obtained by the same method with an average yield of 74%. The phase of both samples was verified by powder X-ray diffraction (XRD) patterns (Fig. S1). The optical photographs of [(Et)$_2$MP]PbBr$_3$ and [(Et)$_2$MP]PbI$_3$ are shown in Fig. S3.

2.3. Single-crystal X-ray diffraction structure determination

The single crystal diffraction data was collected using a ROD Synergy Custom diffractometer equipped with a Liquid MetalJet D2 + Ga-$K\alpha$ radiation source ($\lambda = 1.3405$ Å) at 121 K and a Hybrid Pixel Array Detector. The data reduced using the CrysAlisPro software (version 1.171.41.93a). The SCALE3 ABSPACK scaling algorithm was employed to perform an empirical multi-scan absorption correction utilizing spherical harmonics. The structure was solved by direct method in the

Table 2
Selected Bond Lengths (Å) for [(Et)$_2$MP]PbBr$_3$ and [(Et)$_2$MP]PbI$_3$.

Bond	Dist.	Bond	Dist.
Pb1-Br1	3.0035(12)	Pb1-I1	3.3258(8)
Pb1-Br2	2.9694(12)	Pb1-I2	3.2602(9)
Pb1-Br3	2.8073(15)	Pb1-I3	3.1521(8)
Pb1-Br4	3.1947(13)	Pb1-I4	3.2409(8)
Pb1-Br5	3.1327(12)	Pb1-I5	3.0491(7)
Pb1-Br6	3.2991(13)	Pb1-I6	3.4105(7)

Table 3
Selected bond angles (°) for [(Et)$_2$MP]PbBr$_3$ and [(Et)$_2$MP]PbI$_3$.

Angle	(°)	Angle	(°)
Br1-Pb1-Br2	90.67(3)	I1-Pb1-I2	110.17(14)
Br1-Pb1-Br3	89.07(4)	I1-Pb1-I3	100.90(2)
Br1-Pb1-Br4	169.64(4)	I1-Pb1-I4	88.15(18)
Br1-Pb1-Br5	91.91(3)	I1-Pb1-I5	94.90(2)
Br2-Pb1-Br3	92.20(4)	I2-Pb1-I4	173.35(2)
Br2-Pb1-Br4	91.32(3)	I2-Pb1-I5	99.00(2)
Br2-Pb1-Br5	169.31(4)	I2-Pb1-I6	89.52(19)
Br3-Pb1-Br4	101.01(4)	I3-Pb1-I4	91.90(2)
Br3-Pb1-Br5	98.22(4)	I3-Pb1-I5	91.02(2)
Br5-Pb1-Br6	84.34(3)	I5-Pb1-I6	171.21(2)

ShelXT program and refined by the full-matrix least-squares method using the ShelXL program. The ShelXT and ShelXL programs used are included in OlexSys Olex2 software package (version 1.5) [37–39]. Non-hydrogen atoms were generated based on the different Fourier maps. All non-hydrogen atoms were refined anisotropically. Hydrogen atoms were added to the structure model geometrically and refined with the parent atoms. Table 1 contains detailed crystallographic information (CCDC number: 2239879, 2239870), and Tables 2 and 3 show selected bond lengths and angles.

2.4. Characterization methods and test instruments

Powder X-ray diffraction (PXRD) of samples was collected and recorded by Rigaku Smartlab X-ray (Cu Kα, $\lambda = 1.5406$ Å) at a scanning speed of 5° min^{-1} (the 2θ range is 5–50° and the step size is 0.02° / 2θ). The simulation curves of [(Et)$_2$MP]PbBr$_3$ and [(Et)$_2$MP]PbI$_3$ were calculated and fitted by Mercury Version 2020.1 software. The FT-IR spectra were obtained on the Bruker VERTEX70FT-IR spectrometer using spectral pure potassium bromide and a small number of samples in the range of 4000 cm^{-1} –400 cm^{-1}. Under the background of pure spectral BaSO$_4$, the UV–visible diffuse reflectance spectra were collected using a PerkinElmer-Lambda-950 (USA) UV/VIS/NIR spectrophotometers equipped with an integrating sphere and operated by a computer, and a limited number of powder samples were loaded on the BaSO$_4$. The ultraviolet–visible diffuse reflectance spectrum (DRS) was measured in the 200–800 nm range. Thermogravimetric analysis (TGA) was measured using a NETZSCHSTA449C analyser (Germany) using an Al$_2$O$_3$ crucible with a heating rate of 10 K min^{-1} from 30 to 800 °C and a synthetic air flow rate of 20 mL min^{-1}. The electrical measurements were performed using a Keithley 4200 (USA). Gas sensing related electrical tests with Keithley 2602b (USA) and the labVIEW software written by ourselves. The gas adsorption was measured using MEMS cantilever (LoC-TGA 3000) chips connected to the computer and a Molecular Adsorption Analyzer that was acquired from High-End MEMS Technology Co., Ltd.

3. Results and discussion

3.1. Crystal structure analysis of [(Et)$_2$MP]PbBr$_3$ and [(Et)$_2$MP]PbI$_3$

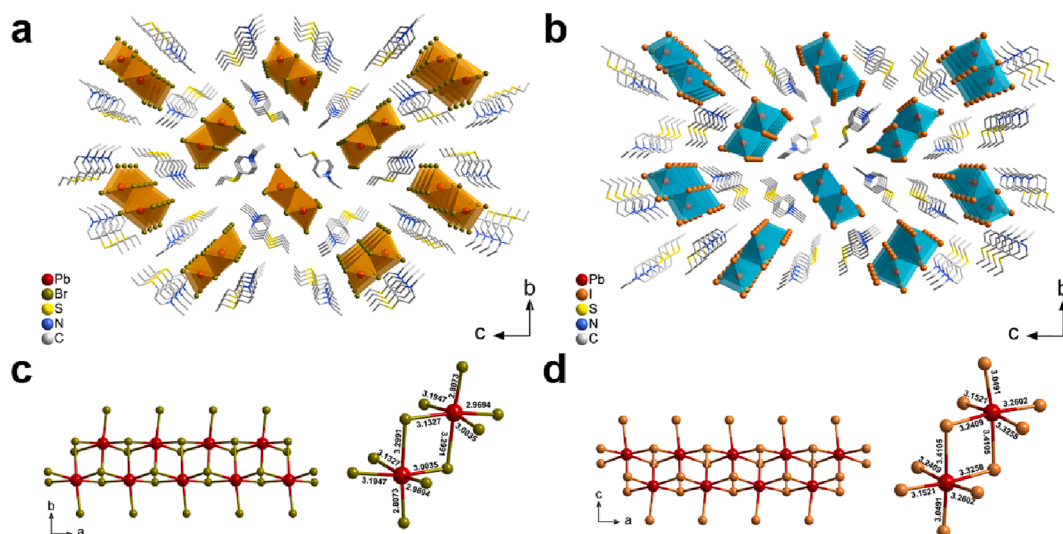During hydrothermal synthesis, p-mercaptopyridines (MP) were

Fig. 1. Crystal structures. Bulk structure view of (a) [(Et)$_2$MP]PbBr$_3$ and (b) [(Et)$_2$MP]PbI$_3$ along the *a*-axis (the hydrogen atoms are omitted for clarity). 1D inorganic chain structure and octahedral of (c) [(Et)$_2$MP]PbBr$_3$ and (d) [(Et)$_2$MP]PbI$_3$. Bond length unit: Å.
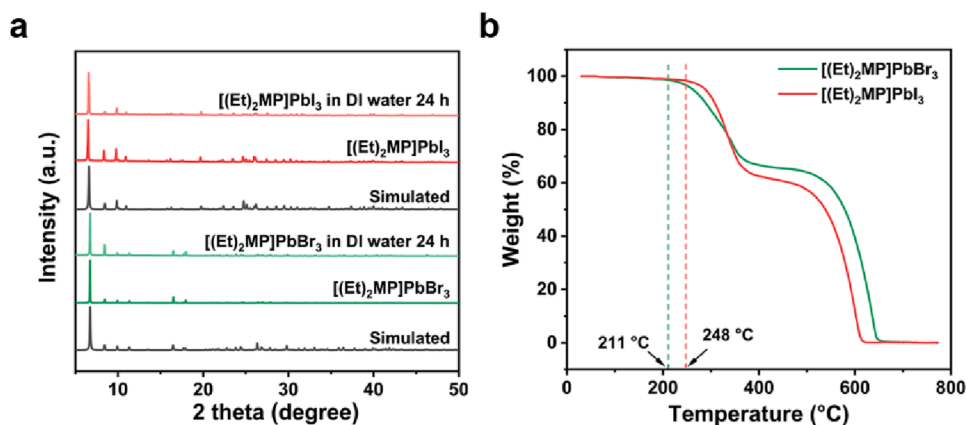

Fig. 2. (a) Water stability and (b) thermal stability of [(Et)$_2$MP]PbBr$_3$ and [(Et)$_2$MP]PbI$_3$.

formed from 4,4′-Dithiodipyridine (DTDP) through disulfide bond breakage. Ethanol acts as an alkylation reagent, converting *p*-mercaptopyridine to [(Et)$_2$MP]$^+$, which served as a cationic templating agent for the formation of one-dimensional inorganic chains [40]. [(Et)$_2$MP]PbI$_3$ is almost identical to [(Et)$_2$MP]PbBr$_3$ in structure with a minor difference in the alignment of organic cations. [(Et)$_2$MP]PbBr$_3$ crystallizes in monoclinic systems with a space group of *P2$_1$2$_1$2$_1$*, where the 1D inorganic [PbBr$_3$]$^-$ chains are balanced by organic [(Et)$_2$MP]$^+$ cations. As shown in Fig. 1c, the Pb^{2+} ion is coordinated by six Br atoms to form an octahedral unit with Pb-Br bond lengths in the range of 2.8073(15)–
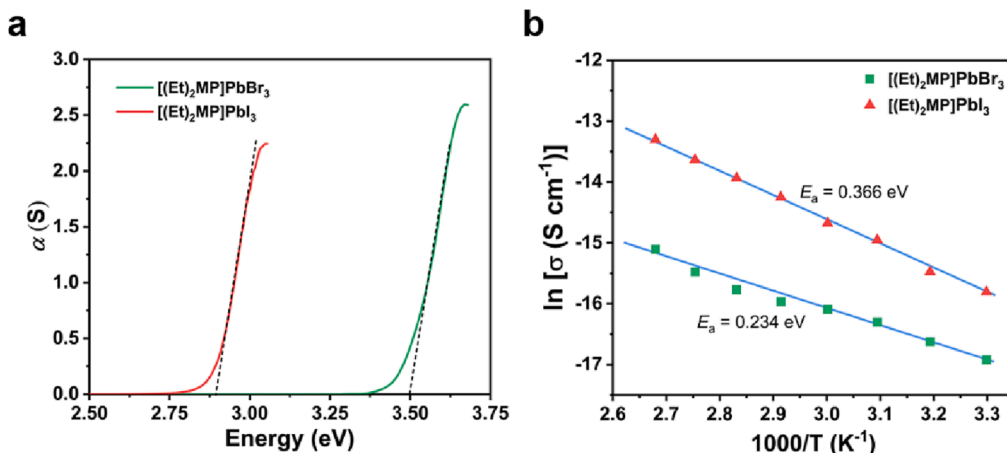

Fig. 3. (a) Optical absorption spectrum and (b) fitting of conductivity at varied temperatures to Arrhenius equation of [(Et)$_2$MP]PbBr$_3$ and [(Et)$_2$MP]PbI$_3$.
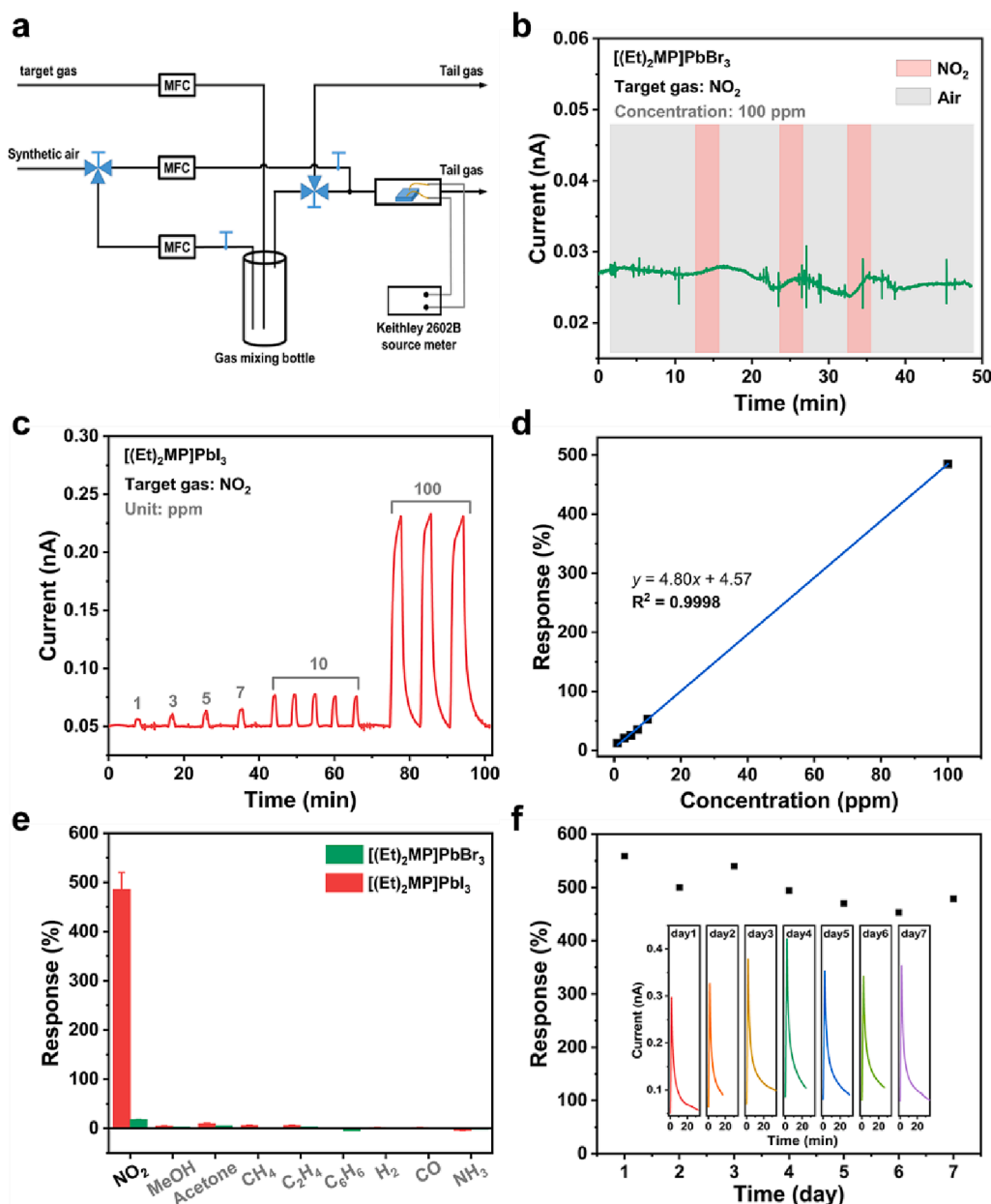
Fig. 4. (a) homemade instrument system for gas sensing test. (b) NO$_2$ response/recovery curve of [(Et)$_2$MP]PbBr$_3$. (c) NO$_2$ Response-concentration scatter plots of [(Et)$_2$MP]PbI$_3$ and (d) linear fits. (e) Response of [(Et)$_2$MP]PbBr$_3$ and [(Et)$_2$MP]PbI$_3$ to different gases in 100 ppm. (f) Long-term stability of [(Et)$_2$MP]PbI$_3$ to NO$_2$ within 7 days (inset curves are the real-time measurement).

3.1947(13) Å. Each [PbBr$_6$] octahedron connects with four adjacent ones through edge-sharing to form a continuous 1D chain extending along the *a*-axis. The organic cations are cleverly distributed around the conductive 1D inorganic chains. The experimental powder XRD spectra of both compounds correspond well with those predicted from their crystal structures (Fig. S1).

3.2. Solvent stability and thermal stability

The water stability of organic–inorganic metal halide hybrids is of great interest [41,42]. Therefore, the crystals were transferred to deionized water for 24 h and the powder XRD patterns were analyzed after that. The result indicated that [(Et)$_2$MP]PbBr$_3$ and [(Et)$_2$MP]PbI$_3$ have good stability in water (Fig. 2a). Moreover, [(Et)$_2$MP]PbBr$_3$ and [(Et)$_2$MP]PbI$_3$ demonstrated high stability by similar treatment in methanol, ethanol, acetonitrile, acetone and dichloromethane (Fig. S4).

Thermogravimetric (TG) analysis shows that [(Et)$_2$MP]PbBr$_3$ initially loses weight at 210 °C under an air flow rate (Fig. 2b). Especially for [(Et)$_2$MP]PbI$_3$, the structure will not collapse before 248 °C, indicating the outstanding stability of [(Et)$_2$MP]PbBr$_3$ and [(Et)$_2$MP]PbI$_3$.

3.3. Semiconductor characteristics

Optical and electrical tests were performed to characterize the semiconductor properties of [(Et)$_2$MP]PbBr$_3$ and [(Et)$_2$MP]PbI$_3$. The Kubelka-Munk formula estimates the optical band gap of [(Et)$_2$MP]PbBr$_3$ and [(Et)$_2$MP]PbI$_3$ to be 3.50 eV and 2.90 eV through ultraviolet–visible diffuse reflectance spectroscopy (Fig. 3a). This suggests that [(Et)$_2$MP]PbBr$_3$ and [(Et)$_2$MP]PbI$_3$ are potential semiconductor materials.

The conductivity of the single crystals of [(Et)$_2$MP]PbBr$_3$ and [(Et)$_2$MP]PbI$_3$ was then measured at various temperatures. The

measured I-V curves display excellent linearity, demonstrating perfect Ohmic contact between the material and electrode [43]. Fig. S5a shows the conductivity rises exponentially as the temperature rises steadily, demonstrating their typical semiconductor features. At room temperature, [(Et)$_2$MP]PbBr$_3$ and [(Et)$_2$MP]PbI$_3$ show conductivities of 4.48 × 10^{-8} and 1.37 × 10^{-7} S cm^{-1} (Fig. S5b), respectively. The activation energies (Ea) of [(Et)$_2$MP]PbBr$_3$ and [(Et)$_2$MP]PbI$_3$ can be approximated to be 0.234 and 0.366 eV using *lnσ-1000/T* plots fitted to straight lines based on the variant of Arrhenius equation (Fig. 3b) [31,44].

3.4. NO$_2$ sensing of [(Et)$_2$MP]PbBr$_3$ and [(Et)$_2$MP]PbI$_3$

Assessing the levels of gaseous pollutants is crucial for understanding their effects on human health, particularly in the context of COVID-19 pandemic. Among these pollutants, NO$_2$ is extremely harmful to humans. Long-term exposure to NO$_2$ can lead to chronic poisoning, polyneuritis, atherosclerosis and other diseases. Therefore, the accurate detection of NO$_2$ is of great importance for our daily life [45–48]. To evaluate the NO$_2$ sensing performances of [(Et)$_2$MP]PbBr$_3$ and [(Et)$_2$MP]PbI$_3$, the crystals were ground into powder and dispersed in ethanol, then loaded the powder onto silver palladium fork finger electrodes with a channel width of 200 μm using a drop-coating method, and the current signals of the devices were collected when exposed to different gas (The devices were shown in Fig. S6). The details are as follows: the sensing performances of [(Et)$_2$MP]PbBr$_3$ and [(Et)$_2$MP]PbI$_3$ towards all gases were evaluated using a homemade instrument system that was developed in an earlier work [49]. The system, as shown in Fig. 4a, consists of piping, a gas mixing device, a test chamber (a quartz tube), and a digital source meter. The prepared devices were placed in the closed quartz tube. Synthetic air (79% nitrogen + 21% oxygen) was selected as the purge and standard carrier gas to simulate the actual operating conditions of the device. The gas flow of air and the target gas was controlled at 600 sccm by mass flow controllers (MFC). Prior to the test, the purge gas was introduced for 1 h to remove any other gas molecules that might be adsorbed on the material surface and to stabilize the baseline. Keithley 2602B Sourcemeter was used to record the electrical signal in real-time. When exposed to NO$_2$, the changes in the current of device were detected. The ratio of current in the target gas atmosphere (I_1) to air current (I_0) was used to calculate the response value (R):

$$R_{response} = (I_1/I_0 - -1) \times 100\% \tag{1}$$

And the sensitivity S is defined as:

$$S = R_{response}/c \tag{2}$$

c is the concentration of target gases.

As shown in Fig. 4b, the $R_{response}$ of [(Et)$_2$MP]PbBr$_3$ to 100 ppm NO$_2$ is about 18.2%. Then, the gas sensing to 100 ppm of different gas for [(Et)$_2$MP]PbBr$_3$ was tested at room temperature and the results were shown in Fig. 4e. It can be seen that [(Et)$_2$MP]PbBr$_3$ is highly inert to other gases, indicating its ultra-high selectivity for NO$_2$.

It is noteworthy that replacing Br atom in the [(Et)$_2$MP]PbBr$_3$ crystal with I atom can significantly enhance the sensitivity of [(Et)$_2$MP]PbI$_3$ to NO$_2$. The current of [(Et)$_2$MP]PbI$_3$ rapidly rose within 2 min upon exposure to NO$_2$. And the real-time dynamic NO$_2$ response/recovery curve of [(Et)$_2$MP]PbI$_3$ is shown in Fig. 4c, demonstrating an excellent response/recovery ability to a broad range of NO$_2$ (1–100 ppm) at room temperature. The $R_{response}$ to 100 ppm NO$_2$ is remarkably high as 490% ($S = 0.126$ ppm^{-1}), which is about 27 times higher than that of [(Et)$_2$MP]PbBr$_3$ to 100 ppm NO$_2$.Moreover, [(Et)$_2$MP]PbI$_3$ exhibits good long-term stability (Fig. 4f). Plotting the response values against NO$_2$ concentrations on a Cartesian coordinate shows good linearity, which can be used to predict the concentration of NO$_2$ in gas sensing (Fig. 4d). In addition, [(Et)$_2$MP]PbI$_3$ was found to be very stable to NO$_2$ sensing at room temperature, with a coefficient of variation of 7.9% for

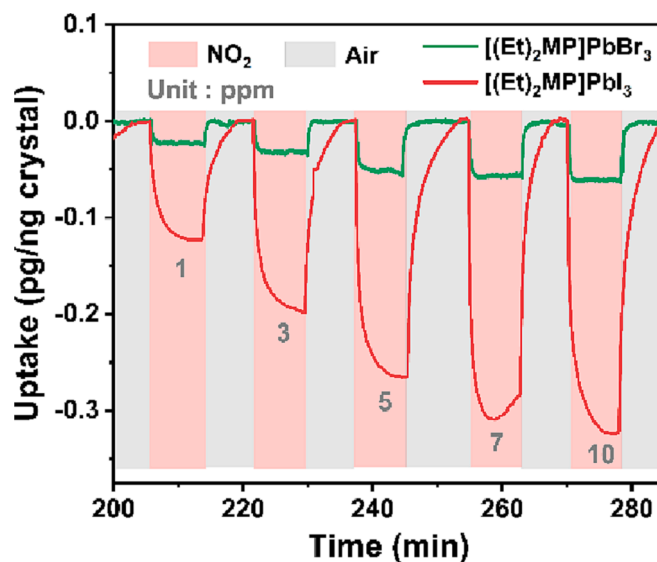**Fig. 5.** NO$_2$ adsorption of [(Et)$_2$MP]PbI$_3$ and [(Et)$_2$MP]PbBr$_3$ from 1 to 10 ppm.

10 ppm NO$_2$ response (Fig. S7).

In addition, the selectivity of [(Et)$_2$MP]PbI$_3$ was evaluated by measuring sensing tests to 100 ppm of methanol, acetone, methane, ethylene, benzene, hydrogen, carbon monoxide, and ammonia, respectively. As shown in Fig. 4e, the material is ultra-selective for NO$_2$ and largely negligible for the other gases. Therefore, [(Et)$_2$MP]PbI$_3$ retains ultra-high selectivity for nitrogen dioxide before and after halogen replacement and increases sensitivity by 2692%, demonstrating the effectiveness of this strategy for improving gas response sensitivity and highlights the great potential of organic–inorganic metal halide hybrids in gas sensing.

3.5. The mechanism of NO$_2$ sensing

The gas-sensitive mechanism of organic–inorganic metal halide hybrids has been discussed in a number of papers [25–27]. Similar to MAPbI$_3$ [26], the surface adsorption of the gas onto [(Et)$_2$MP]PbI$_3$ is a prerequisite for gas sensing. Then NO$_2$ adsorbs on the surface of [(Et)$_2$MP]PbI$_3$ results in a transfer of electrons to the surface, reducing the resistance. The sensitivity of the material to the detected gas is determined by the Lewis alkalinity of the material, which refers to its electron-donating capacity. Since I has a stronger Lewis alkalinity than Br [50–53], [(Et)$_2$MP]PbI$_3$ exhibits higher NO$_2$ adsorption and sensitivity compared to [(Et)$_2$MP]PbBr$_3$. The NO$_2$ adsorption of [(Et)$_2$MP]PbI$_3$ is 0.32 pg of NO$_2$ per ng of material in 10 ppm NO$_2$, whereas that of [(Et)$_2$MP]PbBr$_3$ is only 0.06 pg (see Fig. 5 and supporting information for details). Thus, the stronger NO$_2$ adsorption of [(Et)$_2$MP]PbI$_3$ results in stronger sensitivity of the material.

4. Conclusions

In summary, we have synthesized two new 1D edge-shared organic–inorganic metal halide hybrids with excellent water stability. [(Et)$_2$MP]PbBr$_3$ demonstrated a high selectivity to 100 ppm NO$_2$ with $R_{response}$ of 18.2%. This value can be dramatically increased to 490% (27 times as before) when the bromine in [(Et)$_2$MP]PbBr$_3$ was replaced with iodine. Besides ultra-high selectivity to NO$_2$, [(Et)$_2$MP]PbI$_3$ also exhibits excellent cycling stability. Study of gas-sensitive mechanism reveals that the electron-giving capacity (Lewis alkalinity) of [(Et)$_2$MP]PbI$_3$ is about 5 times stronger than that of [(Et)$_2$MP]PbBr$_3$, resulting in a higher tendency for NO$_2$ interaction and increased gas sensitivity. [(Et)$_2$MP]PbBr$_3$ and [(Et)$_2$MP]PbI$_3$ demonstrate a good example of the

customization of gas-sensitive materials in organic–inorganic metal halide hybrids, showing great potential in the field of gas sensing.

CRediT authorship contribution statement

Jie Chen: Conceptualization, Methodology, Software, Formal analysis, Investigation, Writing – original draft, Visualization. **Chuanzhe Wang:** Software, Formal analysis, Data curation, Validation. **Jianqiang Zhao:** Software, Formal analysis. **Guangling Liang:** Data curation. **Gang Xu:** Supervision, Funding acquisition, Resources, Project administration. **Guan-E Wang:** Supervision, Funding acquisition, Resources, Writing – review & editing.

Declaration of Competing Interest

The authors declare that they have no known competing financial interests or personal relationships that could have appeared to influence the work reported in this paper.

Data availability

Data will be made available on request.

Appendix A. Supplementary material

Supplementary data to this article can be found online at https://doi.org/10.1016/j.inoche.2023.110668.

References

[1] C.H. Lin, B. Cheng, T.Y. Li, J.R.D. Retamal, T.C. Wei, H.C. Fu, X. Fang, J.H. He, Orthogonal lithography for halide perovskite optoelectronic nanodevices, ACS Nano 13 (2019) 1168–1176.

[2] D. Shi, V. Adinolfi, R. Comin, M. Yuan, E. Alarousu, A. Buin, Y. Chen, S. Hoogland, A. Rothenberger, K. Katsiev, Y. Losovyj, X. Zhang, P.A. Dowben, O.F. Mohammed, E.H. Sargent, O.M. Bakr, Low trap-state density and long carrier diffusion in organolead trihalide perovskite single crystals, Science 347 (2015) 519–522.

[3] Y. Lee, J. Kwon, E. Hwang, C.H. Ra, W.J. Yoo, J.H. Ahn, J.H. Park, J.H. Cho, High-performance perovskite–graphene hybrid photodetector, Adv. Mater. 27 (2015) 41–46.

[4] Z.Y. Wu, C.M. Ji, S.S. Wang, W.C. Zhang, Y.Y. Wang, L.N. Li, S.G. Zhao, Z.H. Sun, J. H. Luo, (2-Methylpiperidine)PbI3: an ABX3-type organic-inorganic hybrid chain compound and its semiconducting nanowires with photoconductive properties, J. Mater. Chem. C. 5 (2017) 11466–11471.

[5] C.C. Stoumpos, M.G. Kanatzidis, Halide perovskites: poor man's high-performance semiconductors, Adv. Mater. 28 (2016) 5778–5793.

[6] C.H. Lin, C.Y. Kang, T.Z. Wu, C.L.T. Sai, C.W. Sher, X. Guan, P.T. Lee, T. Wu, C. H. Ho, H.C. Kuo, J.H. He, Giant optical anisotropy of perovskite nanowire array films, Adv. Funct. Mater. 30 (2020) 1909275.

[7] G.N. Liu, R.Y. Zhao, B. Xu, Y. Sun, X.M. Jiang, X. Hu, C. Li, Design, synthesis, and photocatalytic application of moisture-stable hybrid lead-free perovskite, ACS Appl. Mater. Interfaces 12 (2020) 54694–54702.

[8] X.Y. Yang, D. Singh, R. Ahuja, Recent advancements and future prospects in ultrathin 2D semiconductor-based photocatalysts for water splitting 10 (2020) 1111–1160.

[9] C.C. Chen, W.H. Ma, J.C. Zhao, Semiconductor-mediated photo-degradation of pollutants under visible-light irradiation, Chem. Soc. Rev. 39 (2010) 4206–4219.

[10] H.P. Lv, Z.K. Xu, H. Yu, C.R. Huang, Z.X. Wang, A photochromic organic–inorganic hybrid schiff base metal halide ferroelectric, Chem. Mater. 34 (2022) 1737–1745.

[11] Z.Y. Wu, S.N. Li, Y.M. Yousry, W.D. Wong, X.Y. Wang, T. Ma, Z.F. Chen, Y. Shao, W.H. Liew, K. Yao, F. Pan, K.P. Loh, intercalation-driven ferroelectric-to-ferroelastic conversion in a layered hybrid perovskite crystal, Nat. Commun. 13 (2022) 3104–3111.

[12] Z. Sun, A. Zeb, S. Liu, C. Ji, T. Khan, L. Li, M. Hong, J. Luo, Exploring a lead-free semiconducting hybrid ferroelectric with a zero-dimensional perovskite-like structure, Angew. Chem. Int. Ed. 55 (2016) 11854–11858.

[13] Y.F. Miao, X.T. Wang, H.J. Zhang, T.Y. Zhang, N. Wei, X.M. Liu, Y.T. Chen, J. Chen, Y.X. Zhao, In situ growth of atomic layer perovskitoid to stabilize and passivate MAPbI3 for efficient and stable photovoltaics, eScience 1 (2021) 91–97.

[14] R.K. Misra, S. Aharon, B. Li, D. Mogilyansky, I.V. Fisher, L. Etgar, E.A. Katz, Temperature- and component-dependent degradation of perovskite photovoltaic materials under concentrated sunlight, J. Phys. Chem. Lett. 6 (2015) 326–330.

[15] H. Choi, J. Jeong, H. Kim, S. Kim, B. Walker, G. Kim, J.Y. Kim, Cesium-doped methylammonium lead iodide perovskite light absorber for hybrid solar cells, Nano Energy 7 (2014) 80–85.

[16] S. Seo, S. Jeong, C. Bae, N. Park, H. Shin, Perovskite solar cells with inorganic electron- and hole-transport layers exhibiting long-term (≈500 h) stability at 85 °C under continuous 1 sun illumination in ambient air, Adv. Mater. 30 (2018) 1801010.

[17] J.C. Sun, J. Wu, X. Tong, F. Lin, Y.N. Wang, Z.M. Wang, Organic/inorganic metal halide perovskite optoelectronic devices beyond solar cells, Adv. Sci. 5 (2018) 1700780.

[18] H.R. Jia, H.Y. Ma, X.Y. Liu, D.H. Xu, T. Yuan, C. Zou, Z.A. Tan, Engineering organic-inorganic perovskite planar heterojunction for efficient carbon dots based light-emitting diodes, Appl. Phys. Rev. 9 (2022), 021406.

[19] L.X. Hong, W.T. Huang, Z. Bao, Y.S. Chen, R.S. Liu, Stable luminous organic-inorganic hybrid manganese halide nanostructures for light-emitting diodes, ACS Appl. Nano Mater. 5 (2022) 4623–4628.

[20] A.V. Artem'ev, M.P. Davydova, A.S. Berezin, D.G. Samsonenko, I.Y. Bagryanskaya, V.K. Brel, X. Hei, K.A. Brylev, O.I. Artyushin, I.I. Shishkin, J. Li, New approach toward dual-emissive organic–inorganic hybrids by integrating Mn(II) and Cu(I) emission centers in ionic crystals, ACS Appl. Mater. Interfaces 14 (2022) 31000–31009.

[21] Q. Jiang, L.Q. Zhang, H.L. Wang, X.L. Yang, J.H. Meng, H. Liu, Z.G. Yin, J.L. Wu, X. W. Zhang, J.B. You, Enhanced electron extraction using SnO2 for high-efficiency planar-structure HC(NH2)2PbI3-based perovskite solar cells, Nat. Energy 2 (2016) 16177.

[22] E. Horvath, M. Spina, Z. Szekrenyes, K. Kamaras, R. Gaal, D. Gachet, L. Forro, Nanowires of methylammonium lead iodide (CH3NH3PbI3) prepared by low temperature solution-mediated crystallization, Nano Lett. 14 (2014) 6761–6766.

[23] P.C. Zhu, S. Gu, X.P. Shen, N. Xu, Y.L. Tan, S.D. Zhuang, Y. Deng, Z.D. Lu, Z. L. Wang, J. Zhu, Direct conversion of perovskite thin films into nanowires with kinetic control for flexible optoelectronic devices, Nano Lett. 16 (2016) 871–876.

[24] M. Stoeckel, M. Gobbi, S. Bonacchi, F. Liscio, L. Ferlauto, E. Orgiu, P. Samorì, Reversible, fast, and wide-range oxygen sensor based on nanostructured organometal halide perovskite, Adv. Mater. 29 (2017) 1702469.

[25] G.Y. Lee, M.Y. Yang, D.H. Kim, J. Lim, J. Byun, D.S. Choi, H.J. Lee, Y.S. Nam, I. Kim, S.O. Kim, Nitrogen-dopant-induced organic-inorganic hybrid perovskite crystal growth on carbon nanotubes, Adv. Funct. Mater. 30 (2019) 1902489.

[26] G. Kakavelakis, E. Gagaoudakis, K. Petridis, V. Petromichelaki, V. Binas, G. Kiriakidis, E. Kymakis, Solution processed CH3NH3PbI3-xClx perovskite based self-powered ozone sensing element operated at room temperature, ACS Sens. 3 (2018) 135–142.

[27] D.Y. Li, J.H. Song, Y. Cheng, X.M. Wu, Y.Y. Wang, C.J. Sun, C.-Y. Yue, X.W. Lei, Ultra-sensitive, selective and repeatable fluorescence sensor for methanol based on a highly emissive 0D hybrid lead-free perovskite, Angew. Chem. Int. Ed. 61 (2022) e202206437.

[28] C. Muthu, S.R. Nagamma, V.C. Nair, Luminescent hybrid perovskite nanoparticles as a new platform for selective detection of 2,4,6-trinitrophenol, RSC Adv. 4 (2014) 55908–55911.

[29] G.Q. Huang, H.L. Zhou, C.P. Wang, C. Kashi, X.L. Ye, W.H. Li, G.E. Wang, G. Xu, A new 1D inorganic-organic hybrid perovskite-like semiconductor with high stability and humidity response, Inorg. Chem. Commun. 128 (2021) 108581–108587.

[30] M.E. Franke, T.J. Koplin, U. Simon, Metal and metal oxide nanoparticles in chemiresistors: does the nanoscale matter? Small 2 (2006) 36–50.

[31] M. Tiemann, Porous metal oxides as gas sensors, Chem. Eur. J. 13 (2007) 8376–8388.

[32] G. Korotcenkov, The role of morphology and crystallographic structure of metal oxides in response of conductometric-type gas sensors, Mater. Sci. Eng. R 61 (2008) 1–39.

[33] T.T. Liang, Z.F. Dai, Y.D. Liu, X. Zhang, H.B. Zeng, Suppression of Sn2+ and Lewis acidity in SnS2/black phosphorus heterostructure for ppb-level room temperature NO2 gas sensor, Sci. Bull. 66 (2021) 2471–2478.

[34] H.J. Jiang, L.A. Cao, Y.Z. Li, A.W.H. Li, X.L. Ye, W.H. Deng, X.M. Jiang, G.E. Wang, G. Xu, Organic "receptor" fully covered few-layer organic–metal chalcogenides for high-performance chemiresistive gas sensing at room temperature, Chem. Commun. 56 (2020) 5366–5369.

[35] M. Hoffmann, L. Mayrhofer, O. Casals, L. Caccamo, F. Hernandez-Ramirez, Ge. Lilienkamp, W. Daum, M. Moseler, A. Waag, H. Shen, J. Prades, A highly selective and self-powered gas sensor via organic surface functionalization of p-Si/ n-ZnO diodes, Adv. Mater. 26 (2014) 8017–8022.

[36] Z.J. Tan, Y. Wu, H. Hong, J.B. Yin, J.C. Zhang, L. Lin, M.Z. Wang, X. Sun, L.Z. Sun, Y.C. Huang, K.H. Liu, Z.F. Liu, H.L. Peng, Two-dimensional (C4H9NH3)2PbBr 4 perovskite crystals for high-performance photodetector, J. Am. Chem. Soc. 138 (2016) 16612–16615.

[37] G.M. Sheldrick, SHELXT-integrated space-group and crystal-structure determination, Acta Crystallogr. Sect. A-Found. Adv. 71 (2015) 3–8.

[38] G.M. Sheldrick, Crystal structure refinement with SHELXL, Acta Crystallogr. Sect. C-Struct. Chem. 71 (1) (2015) 3–8.

[39] O.V. Dolomanov, A.J. Blake, N.R. Champness, M. Schroder, OLEX: new software for visualization and analysis of extended crystal structures, J. Appl. Crystallogr. 36 (2003) 1283–1284.

[40] C.Y. Yue, N. Lin, L. Gao, Y.X. Jin, Z.Y. Liu, Y.Y. Cao, S.S. Han, X.K. Lian, B. Hu, X. W. Lei, Organic cation directed one-dimensional cuprous halide compounds: syntheses, crystal structures and photoluminescence properties, Dalton Trans. 48 (2019) 10151–10159.

[41] G.N. Liu, R.Y. Zhao, R.D. Xu, Q. Liu, B. Xu, Y.Y. Wang, Q. Wu, J.N. Wang, Y. Nie, C. Li, Constructing moisture-stable hybrid lead iodine semiconductors based on hydrogen-bond-free and dual-iodine strategies, J. Mater. Chem. C 7 (2019) 7700–7707.

[42] Z.R. Zhao, F.D. Gu, H.X. Rao, S.Y. Ye, Z.W. Liu, Z.Q. Bian, C.H. Huang, Metal halide perovskite materials for solar cells with long-term stability, Adv. Energy Mater. 9 (2019) 1802671.

[43] M.S. Yao, W.H. Li, G. Xu, Metal-organic frameworks and their derivatives for electrically-transduced gas sensors, Coord. Chem. Rev. 426 (2021), 213479.

[44] S.H. Sun, Q.C. Zhang, X.L. Ye, C.E. Kashi, W.H. Li, G.E. Wang, G. Xu, High-humidity sensor of a new trinuclear Ti-3-Oxo cluster, Chin. J. Struct. Chem. 41 (2022) 2203070–2203076.

[45] X. Zhou, S.Y. Lee, Z.C. Xu, J.Y. Yoon, Recent progress on the development of chemosensors for gases, Chem. Rev. 115 (2015) 7944–8000.

[46] R. Kumar, O. Al-Dossary, G. Kumar, A. Umar, Zinc oxide nanostructures for NO_2 gas–sensor applications: a review, Nano-Micro Lett. 7 (2015) 97–120.

[47] J. Kong, N.R. Franklin, C.W. Zhou, M.G. Chapline, S. Peng, K. Cho, H.J. Dai, Nanotube molecular wires as chemical sensors, Science 287 (2000) 622–625.

[48] K. Wetchakun, T. Samerjai, N. Tamaekong, C. Liewhiran, C. Siriwong, V. Kruefu, A. Wisitsoraat, A. Tuantranont, S. Phanichphant, Semiconducting metal oxides as sensors for environmentally hazardous gases, Sens. Actuat. B 160 (2011) 580–591.

[49] M.S. Yao, W.X. Tang, G.E. Wang, B. Nath, G. Xu, MOF thin film-coated metal oxide nanowire array: signifi cantly improved chemiresistor sensor performance, Adv. Mater. 28 (2016) 5229–5234.

[50] T. Marcelli, Mechanistic insights into direct amide bond formation catalyzed by boronic acids: halogens as Lewis bases, Angew. Chem. Int. Ed. 49 (2010) 6840–6843.

[51] M.H. Stefan, J.I. Elisa, M.U. Jesus, I. Ivan, Unexpected trends in halogen-bond based noncovalent adducts, Chem. Commun. 48 (2012) 7708–7710.

[52] T. Ronny, S.S. Ulrich, Recent advances for halogen bonding in solution: from anion recognition through templated self-assembly to organo-catalysis, Angew. Chem. Int. Ed. 57 (2018) 6004–6016.

[53] G. Somraj, K. Imran, N. Anuradha, S. Govindasamy, Role of Lewis-base-coordinated halogen(I) intermediates in organic synthesis: the journey from unstable intermediates to versatile reagents, Eur. J. Org. Chem. 37 (2017) 5497–5518.